RSC Advances

ROYAL SOCIETY OF CHEMISTRY

www.rsc.org/advances

Three-Dimensional Polymer-Derived Ceramic/Graphene Paper as Li-Ion Battery and Supercapacitor Electrode

L. David †, K. M. Shareef* †, M. A. Abass, and G. Singh*

Mechanical and Nuclear Engineering Department, Kansas State University, Manhattan, Kansas, 66506, United States

* Corresponding author:

K. M. Shareef

Gurpreet Singh

Mechanical and Nuclear Engineering Department, Kansas State University, Manhattan, Kansas, 66506, United States

Tel.: +1-785-532-7085. Fax: +1-785-532-7057

E-mail: muhamed@ksu.edu, gurpreet@ksu.edu

† Denotes equal authorship

Abstract

We study synthesis and electrochemical performance of molecular precursor-derived ceramic (PDC)/carbon nanotube-embedded graphene self-supporting composite papers as Li-ion battery and supercapacitor electrodes. The composite papers are prepared using vacuum filtration of PDC-graphene oxide (GO) dispersion, followed by thermal reduction at 500 ^{o}C. Tested as Li-ion battery electrode, the composite papers deliver reversible capacity as high as 300 mAh g^{-1} (normalized with respect to total mass of electrode) with negligible capacity loss after 1000 charge/discharge cycles. Boron-doped silicon carbon nitride (Si(B)CN) outperforms its undoped counterpart (SiCN) in terms of rate capability, cyclic stability, and coulombic efficiency. Among the PDC materials analyzed, Si(B)CN-CNT-rGO demonstrates the lowest ohmic resistance and highest specific capacitance of approximately 269.52 F g^{-1} at a current density of 5 A g^{-1}, making it a promising electrode material for electrochemical energy storage applications.

Keywords: Polymer-derived ceramics; graphene; composite; electrodes; battery; supercapacitor

1. Introduction

Increasing energy demands of the modern world have motivated research on development of lithium-ion batteries (LIBs) with high energy density, rate capability, and long cycle life. [1–7] Traditionally, graphite has been the chosen anode material for LIBs because of its ability to store and release lithium (Li) between its layers with high cycling efficiency and relatively low volume changes. However, it falls short of today's battery energy demands due to its limited theoretical specific capacity of approximately 370 mAh g^{-1} and a lower reversible capacity at higher current densities (approximately 70 mAh g^{-1} at 100 mA g^{-1}). [8] To this end, silicon (Si) has emerged as an attractive alternative because of its high theoretical gravimetric capacity of approximately 4200 mAh g^{-1} and relatively low discharge potential (approximately 0.5 V versus Li/Li^{+}). [9–17] However, preliminary research of Si anodes has revealed its primary drawback to be the high volume expansion (as much as 400%) during lithiation, causing mechanical and electrical failure of the electrode with increasing number of cycles.[18–23] Although several solutions based on Si-based nanostructures such as nanowires and nanoparticles and Si/C nanocomposites have been proposed, convincing results from a commercial and practical stand-point are yet to be. [24]

In the last decade, Si-based molecular precursor-derived ceramics (PDCs) (such as SiCN, SiAlCN, Si(B)CN etc.) have emerged as promising engineering materials for a number of applications. [25–31] This is mainly due to their high thermodynamic and chemical stability as a result of their amorphous structure, which consists of graphene-like carbon chains wrapped around 10–20 Å-size domains of silicon nitride or silicon carbide (in the case of SiCN ceramic). A relatively more intriguing and emerging property of PDCs is their ability

to reversibly store Li at potentials ranging from 0 to 2.5 V (vs Li/Li^+), offering charge capacity that is more than twice the capacity of commercial graphite at high C-rates while maintaining similar coulombic efficiency. [32–40] Unlike crystalline Si-based anodes, PDCs also generally do not suffer from extreme volume changes due to their less dense (1.8–2.3 g cm^{-3}) and open amorphous structure. However, PDCs-based anodes may have other drawbacks such as: voltage hysteresis, high first-cycle loss, and decreasing capacity at high C-rate, which are generally attributed to their low electrical conductivity and presence of nanovoides, which act as trap for Li atoms. Efforts have been made in the past to improve the electrical conductivity in these materials by increasing the free carbon content in the ceramic by pyrolyzing the precursor at higher temperatures (>1000 °C), but that often leads to electrochemical capacity values similar to or worse than commercial graphite. In this context, boron-modified polymer-derived ceramics such as Si(B)CN are of interest because of their high electrical conductivity (as much as four orders of magnitude higher than SiCN) and robust nanodomain structure, which has a much higher thermodynamic stability than SiCN. [25, 41] Further, chemical interfacing of Si(B)CN with carbon nanotubes (CNTs) also leads to formation of a composite core-shell structure that may improve Li-ion diffusion into the ceramic at high charge/discharge rates, [42–46] act as structural buffer for large volume expansion of the ceramic during cyclic charging and discharging processes, and enhance the ceramic's electrical conductivity and surface area. Finally, by embedding sheets of reduced graphene oxide (rGO) into the Si(B)CN-CNT ceramic, the interconnection between rGO and CNT could also reduce the electrode's internal resistance due to formation of a conductive network that eases electronic transport. [47]

In this work, we measured and compared the Li cyclic ability of Si(B)CN in two design configurations: PDC/graphene (Si(B)CN-rGO) and PDC-nanotube/graphene (Si(B)CN-CNT-rGO), for more than 1000 electrochemical cycles, and also investigated the supercapacitance electrochemical properties of Si(B)CN-CNT-rGO due to its lower ohmic resistance compared to other PDCs.

Unlike traditional electrode materials that use conducting agents, polymeric binders, and copper current collector foil (all of which contribute to approximately 10% of the total cell weight), these composite paper electrodes were self-supporting and were synthesized by vacuum filtration of dispersions consisting of active phase (PDC or PDC-nanotube) in graphene oxide (GO) in deionized (DI) water, followed by thermal reduction of GO to rGO. The rGO serves as a highly crumpled (porous), mechanically flexible and electrically conductive matrix for the active phase (i.e., PDC nanotubes or particles) in the LIB anode design and supercapacitor electrode.

2. Experimental section

2.1 Materials and Instrumentation

Sodium nitrate ($NaNO_3$, 99.2%), potassium permanganate ($KMnO_4$, 99.4%), sulfuric acid (H_2SO_4, 96.4%), hydrogen peroxide (H_2O_2, 31.3% solution in water), hydrochloric acid (HCl, 30% solution in water), and ethanol (C_2H_5OH, 99.9%) were purchased from Fisher Scientific. Trimethyl borate reagent (99.9%) was purchased from Sigma Aldrich, and Poly(ureamethylvinyl)silazane (Ceraset™) was purchased from Ceraset, Clariant. All materials were used as received without further purification.

Scanning electron microscopy (SEM) of the synthesized material was carried out on a Carl Zeiss EVO MA10 system with incident voltage of 5–30 KV. Transmission electron microscope (TEM) images were digitally acquired using a Phillips CM100 operated at 100 KV. Surface chemical composition was studied using X-ray photoelectron spectroscopy (XPS) (PHI Quantera SXM) with monochromatic Al K_α X-radiation. The oxidative stability and effects of annealing of the composites was studied using Thermogravimetric Analysis (TGA) (Shimadzu 50 TGA). About 2.5 mg of the samples being analyzed were heated in a platinum pan at a heating rate of 10 ^{o}C min^{-1} in air flowing at 10 ml min^{-1}.

2.2 Preparation of graphene oxide

Modified Hummer's method was used to make GO. [48, 49] Typically, concentrated H_2SO_4 (130 mL) was added to a mixture of graphite flakes (3 g) and $NaNO_3$ (1.5 g). Then, the mixture was cooled using an ice bath. $KMnO_4$ was added slowly to this mixture for 12 h at 50 °C. The mixture was then quenched with water (400 mL) containing 30% H_2O_2 (3 mL) while in the ice bath such that the temperature does not exceed 20 °C. The remaining material was washed twice in succession with 200 mL of water, 200 mL of 30% HCl, and 200 mL of C_2H_5OH. Afterwards, the purified material was coagulated with 200 mL of ether (Fisher Scientific) and filtered through a paper filter. The filtrate was dried overnight to obtain dry GO.

2.3 Preparation of Si(B)CN-CNT, SiCN-CNT, and Si(B)CN

Synthesis of Si(B)CN–CNT composite was performed similarly to other PDC–CNT composites described in the literature. [46, 50] Briefly, 1 g of multi-walled carbon nanotubes

(MWCNTs) (C150 HP, Bayer AG) was dispersed in 1 g L^{-1} sodium dodecyl benzene sulfonic acid (NaDDBS) (Sigma Aldrich) aqueous solution, followed by sonication for 1 h to remove unwanted agglomerations. The dispersed nanotubes were then washed repeatedly with DI water to eliminate excess NaDDBS and related impurities, followed by slow drying that yielded a dry CNT mass. These dried nanotubes (approximately 1 g) were dispersed in toluene (125 mL) (99.8%, Macron Fine Chemicals™) for further functionalization with the Si(B)CN polymeric precursor. Commercially sourced poly(ureamethylvinyl)silazane (Ceraset™) was modified using trimethyl borate reagent. The precursor was then slowly added and stirred in the 5 wt. % CNT dispersed in toluene. After stirring the mixture for an approximate duration of 24 h, it was dried in an inert atmosphere at 80 °C. The dried mixture was then transferred to a tube furnace where it was heated to 400 °C for 90 min for cross-linking of the precursor, followed by pyrolysis at 1000 °C for 5 h in a nitrogen (N_2) atmosphere at 5 °C min^{-1} heating and cooling rates to yield Si(B)CN−CNT composite. The same procedure used to synthesize Si(B)CN−CNT composite was adapted to synthesize SiCN-CNT, with the exception that only poly(ureamethylvinyl)silazane (Ceraset™) was used as the polymeric precursor.

The Si(B)CN powder specimen was prepared according to standard procedures described in the literature. [46] Briefly, liquid Ceraset modified with trimethyl borate reagent was cross-linked in a vertical tube furnace at approximately 300 °C in N_2 for 4 h, resulting in an infusible mass that was ball-milled for 2 h and pyrolyzed at 1000 °C for 5 h in N_2, resulting in a fine black Si(B)CN powder.

2.4 Preparation of composite paper

10 mL colloidal suspension of GO in 1:1 (v/v) water was made by sonication for 10 min, and then 60 wt. % active material in 10 mL of isopropanol (ISP) (Fisher Scientific) was added to this solution, which was further sonicated for 60 min. The composite suspension was then filtered via vacuum filtration though a 10 μm filter membrane. The composite paper obtained was carefully removed from the filter paper and dried. This dry paper then underwent reduction by heat treatment in a tube furnace at 500 °C under argon atmosphere for 2 h. The thermal reduction process resulted in the conversion of GO to rGO with approximately 50% weight loss due to loss of hydroxyl and carboxyl groups. [51] Therefore, in the thermally reduced composite paper, the ratio of active material to rGO was approximately 80:20 by weight. The active material here refers to SiCN-CNT, Si(B)CN, Si(B)CN-CNT in SiCN-CNT-rGO, Si(B)CN-rGO, and Si(B)CN-CNT-rGO, respectively. The pyrolyzed paper was used as working electrode for LIB half-cells and supercapacitors.

2.5 LIB cell assembly and testing

Coin-cell assembly comprising of Li half-cell batteries were made by punching circles with diameters of 14.3 mm out of the composite paper for use as working electrodes. Since the electrodes were free-standing, they were not calendared before use. The total electrode mass loading varied from approximately 1.6 to 3.0 mg cm^{-2}. Five drops of electrolyte solution of 1M Lithium hexafluorophosphate ($LiPF_6$) (Alfa Aesar) were dissolved in (1:1 v/v) dimethyl carbonate (Sigma Aldrich): ethylene carbonate (Sigma Aldrich) (ionic conductivity 10.7 mS cm^{-1}), and a 25 μm thick (19 mm diameter) glass separator soaked in electrolyte was placed between the working electrode and pure Li metal (14.3 mm

diameter, 75 μm thick), acting as a counter electrode. Washer, spring, and a top casing were placed on top to complete the assembly before crimping. The entire procedure was carried out in an argon-filled glovebox.

Electrochemical performance of the assembled coin cells was tested using a multichannel BT2000 Arbin test unit sweeping between 2.5 V to 10 mV vs Li/Li^+ using a specified cycle schedule. In the asymmetric mode, Li was inserted at 100 mA g^{-1} (considering the total weight of the electrode), while the extraction was performed at increasing current densities of 100, 200, 400, 800, 1600, and 2400 mA g^{-1} for five cycles each, returning to 100 mA g^{-1} for the next 10 cycles. In the symmetric mode, all cells were subjected to symmetric cycling at a current density of 1600 mA g^{-1} for up to 1000 cycles, returning to 100 mA g^{-1} for the last 10 cycles.

2.6 Supercapacitance electrochemical measurement

The electrochemical performance of the free-standing electrode materials were tested using a two-electrode setup on a CHI660E (CH Instruments, Inc.) electrochemical workstation in 6M potassium hydroxide (KOH, 87.2%, Fisher Scientific) aqueous electrolyte at room temperature. The electrode cell configuration was comprised of a pair of 1 cm^2 of the active material, each weighing 1.1 mg. Both pairs were sandwiched between a Whatmann filter paper pretreated in the electrolyte. Electrochemical impedance spectrum (EIS) of the materials was analyzed with an alternating voltage of 5 mV amplitude in a frequency range of 1 MHz to 10 mHz at open circuit potential (OCP). Based on experimental results, only Si(B)CN-CNT-rGO was subjected to further analysis. The

cyclic voltammetry (CV) and galvanostatic charge-discharge (GCD) of Si(B)CN-CNT-rGO were tested in a potential range of 0–0.6 V at various current densities.

3. Results and discussion

SEM images of ball-milled Si(B)CN, SiCN-CNT, and Si(B)CN-CNT are shown in Fig. S1 (a)–(c). Average particle size for SiCN-CNT was 1–5 μm, while that of Si(B)CN and Si(B)CN-CNT were approximately 5–10 μm. These particles were mixed with GO which was dispersed in ISP/DI water (1:1) and sonicated for 30 min to form a uniform dispersion. By varying the volume of the composite dispersion, the thickness and loading of the resulting free-standing paper electrode can be controlled.

Fig. 1(a) illustrates the schematic of the synthesis procedure. These papers were reduced in argon to convert GO, an electrically non-conducting material, to electrically conducting rGO. Fig. S2 shows the SEM images of (a) Si(B)CN, (b) SiCN-CNT, and (c) Si(B)CN-CNT free-standing composite paper. From Fig. S2, the pore size of the free-standing electrodes varied from 2 to 10 μm while the calculated porosity was in the range of 70 to 80%. The cross-sectional views of the aforementioned materials are shown in Fig. 1 (b)–(d). The resulting particles were uniformly sandwiched between individual graphene sheets during the vacuum filtration process, which results in the formation of a porous, thin, light-weight, mechanically strong, and self-supporting paper. The average paper thickness of these composites was determined to be approximately 20–40 μm. The images show small (1–10 μm) PDC particles covered with large (10–50 μm) GO sheets. Corresponding TEM images in Fig. 1 (e)–(g) confirmed the observations from the SEM imaging. The high resolution TEM images from Fig. 1 (e)–(g) show the SiCN and Si(B)CN coating on nanotubes and their

uniform distribution in the rGO matrix. The insert in Fig. 1(e) shows the selected area electron diffraction (SAED) pattern obtained from the respective points in the image. Spot 1 shows a hexagonal spot pattern indicating that the hexagonal spot pattern was preserved in the lattice after thermal reduction. Spot 2 indicates a pattern that is typical to an amorphous material, specifically Si(B)CN particle. XPS was used to characterize the starting material and composite papers (Fig. S3 (a)-(b)). Silicon (Si2s, Si2p), oxygen (O1s, O2s), and carbon (C1s) peaks present in the ceramic were also observed in the composite papers. Because XPS is a surface analysis technique, the presence of rGO in the free-standing paper resulted in increase in carbon content in the elemental composition (supplementary Table S1) and decrease in boron content in Si(B)CN, Si(B)CN-CNT and Si(B)CN-CNT-rGO. The XPS spectrum of rGO is presented in Fig. S3 (c). As expected, the amount of oxygen functionalities in rGO had reduced to 16 wt. % after annealing. Based on this observation, it can be inferred that amount oxygen functionalities in Si(B)CN-CNT-rGO would reduce. The reduction in the amount of oxygen functionalities in the composite is desirable; as previous studies have shown that high rate capability and low first-cycle loss has a negative correlation with the amount of oxygen functionalities in LIBs. [52]

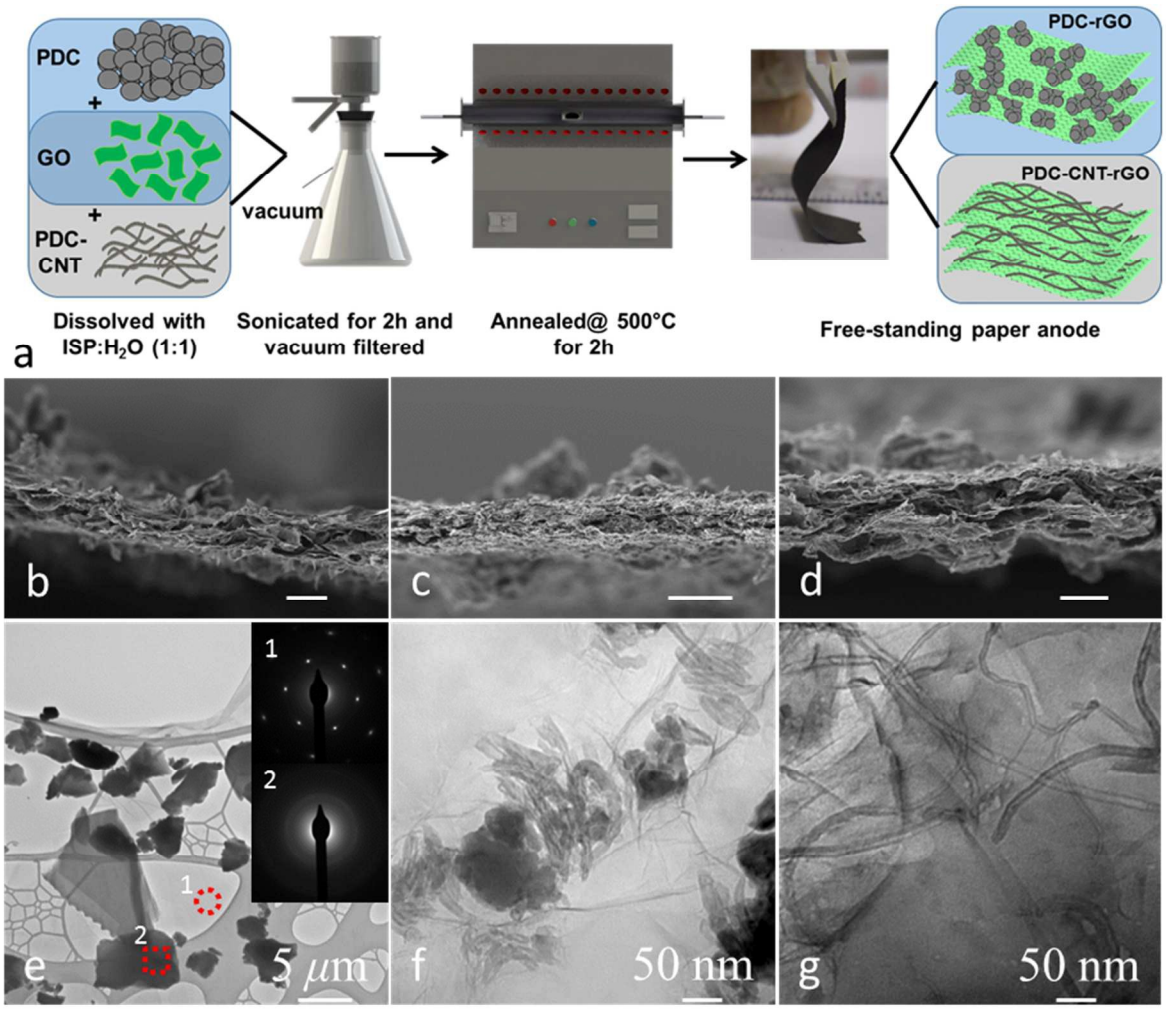

Fig. 1. (a) Schematic showing the synthesis of free-standing composite paper. SEM cross-sectional images of (b) Si(B)CN, (c) SiCN-CNT and (d) Si(B)CN-CNT of the free-standing composite paper. (e)–(g) TEM images of composite paper corresponding to SEM images above. Scale bar is 20 micrometers for (b) through (d).

The loading of active materials in the composite was inferred from Thermo-gravimetric Analysis (TGA) in flowing air at 20-900 °C. Si(B)CN is stable in air up to at least 900 °C. While rGO and CNT tends to burn at ~500 and 600 °C, respectively (as shown in Fig. S4) the active material (Si(B)CN-CNT) tends to burn at a higher temperature (~715 °C) with ~ 74% of its weight remaining after pyrolysis. The stability of Si(B)CN-CNT can be credited to the presence of Si(B)CN ceramic.

Fig. 2 shows the voltage charge-discharge profiles for (a) SiCN-CNT-rGO and (b) Si(B)CN-CNT-rGO composite paper electrodes. The SiCN-CNT-rGO composite electrode showed electrochemical discharge and charge capacity of ~712 mAh $g^{-1}_{electrode}$ and ~342 mAh $g^{-1}_{electrode}$ with relatively low first-cycle loss (48%). However, Si(B)CN-CNT-rGO composite paper had first-cycle discharge and charge capacities of approximately 567.4 and 247 mAh $g^{-1}_{electrode}$ respectively.

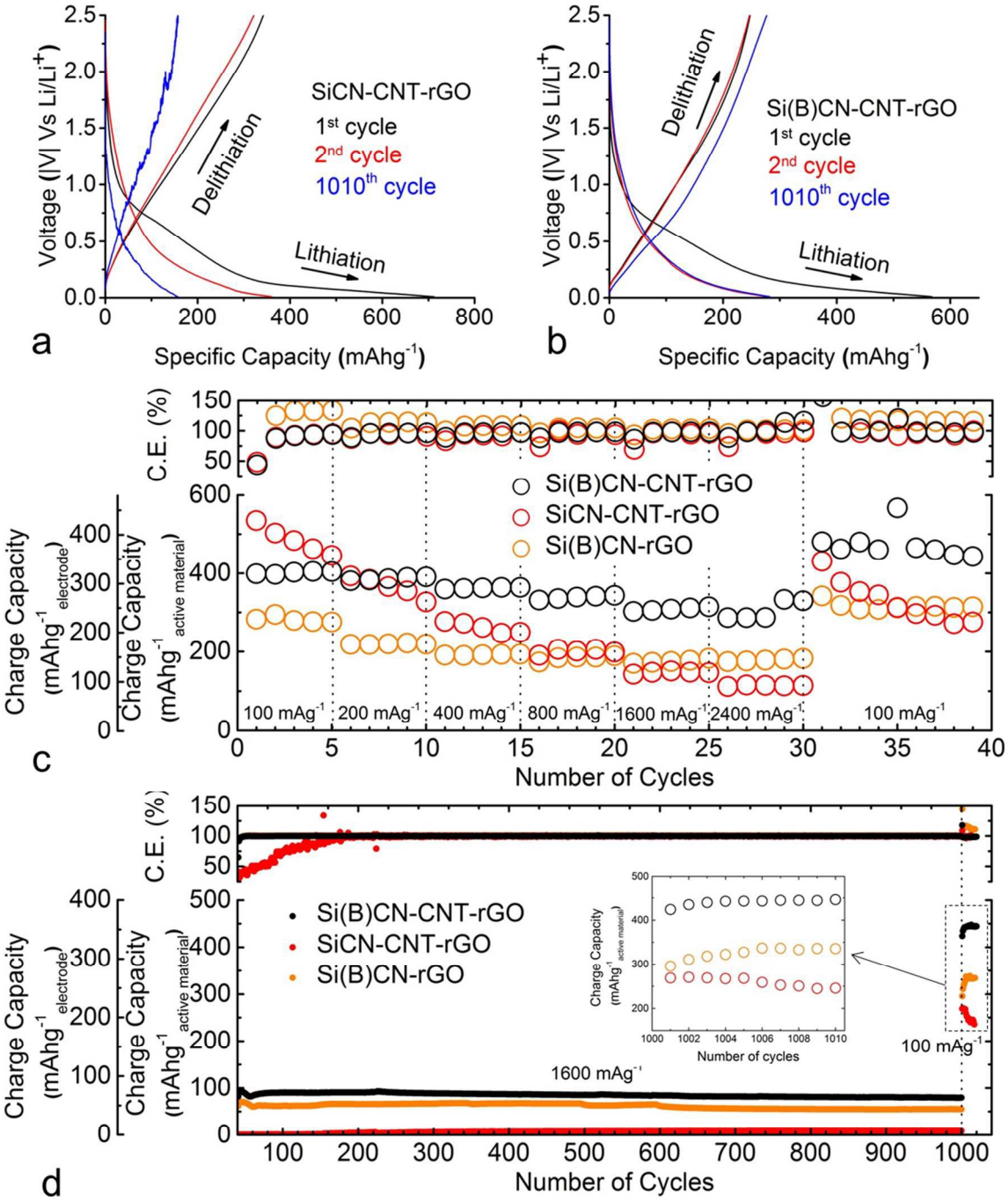

Fig. 2. 1st, 2nd and 1010th cycle voltage profile for (a) SiCN-CNT-rGO and (b) Si(B)CN-CNT-rGO paper electrodes, (c) Charge capacity of all electrodes asymmetrically cycled at different rates along with their cyclic efficiencies, and (d) Charge capacity of all electrodes symmetrically cycled at 1600 mA $g^{-1}{}_{electrode}$ for 1000 cycles.

When these electrodes were further cycled with increasing current density, a slight drop in charge capacity was observed, as shown in Fig. 2(c). At 2400 mA g^{-1}, Si(B)CN-rGO paper capacity dropped to ~146 mAh $g^{-1}{}_{electrode}$, which is ~66% of its reversible charge capacities at 100 mA g^{-1}. The SiCN-CNT-rGO composite paper electrode was the poorest performing electrode, with only ~73 mAh $g^{-1}{}_{electrode}$ (26% retention) charge capacity at 2400 mA g^{-1}, while Si(B)CN-CNT-rGO maintained most of its charge capacity at 211 mAh $g^{-1}{}_{electrode}$ (82% retention). When the cells were cycled back at 100 mA g^{-1}, all the cells regained their initial charge capacities at 218, 275, and 307 mAh $g^{-1}{}_{electrode}$ for Si(B)CN-rGO, SiCN-CNT-rGO, and Si(B)CN-CNT-rGO, respectively. Compared to Si(B)CN-CNT, other PDC-based electrodes reported in the literature, such as SiCN, had first-cycle reversible capacity of 13 mAh g^{-1}, while the MWCNT had first-cycle charge capacity of 210 mAh g^{-1}.[53, 54] In order to test cell performance during long-term cycling, the cells were cycled at 1600 mA g^{-1} during both charge and discharge half cycles (Fig. 2(d)). Si(B)CN-CNT-rGO had a marginally higher charge capacity at ~52 mAh g^{-1} than Si(B)CN-rGO electrode at ~40 mAh g^{-1}, while the SiCN-CNT-rGO cell had no capacity. The Si(B)CN-CNT-rGO electrode cycled with a capacity loss of only 10 % over 1000 cycles. With the exception of SiCN-CNT-rGO, all the other cells regained most of their initial capacity when they were cycled at a current density of 100 mA g^{-1} after 1000 cycles. Si(B)CN-CNT-rGO was the best-performing electrode with a charge capacity of 285 mAh $g^{-1}{}_{electrode}$ (93% retention) at 100 mA g^{-1} after 1000 cycles at 1600 mA g^{-1} during both discharge and charge half cycles. A summary of the properties of the tested electrodes and their performance in relation to some other PDC electrode materials being reported in literature is presented in Table 1.

So far, boron-doped SiCN composites displayed a higher charge capacity at higher currents than their undoped counterpart. This is in agreement with previous studies that have shown that boron doping specifically improves the charge capacity of SiCN-based PDCS. [41] Also, the reinforcement of the Si(B)CN with CNT and rGO is expected to improve its thermal and chemical stability without compromising the mechanical strength and porosity required for applications involving higher charge retention and cyclic performance.

Previous studies on PDC electrodes have shown that voltage hysteresis during Li extraction may be influenced by the amount of residual hydrogen atoms in the ceramic. [55] Based on previous studies, the hydrogen content in PDC composites pyrolyzed at 1000 ^{o}C is expected to be low (< 1 wt. %). For instance, 0.25-0.3 wt. % and less than 1 wt. % have been reported for SiOC [51] and SiCN-based PDCs [56, 57], respectively. More so, the amount of hydrogen in rGO annealed at 200C is is reported to be approximately 0.6 wt. % [58] and therefore, thermal reduction at 500 ^{o}C (in the present study) will amount to even lower residual hydrogen. Hence, the contribution of hydrogen towards the charge capacity and cyclability of the composite paper electrode may be discounted.

Table 1 Comparison of properties of Si(B)CN-rGO, SiCN-CNT-rGO, and Si(B)CN-CNT-rGO free-standing paper

Electrode type	Specimen	Charge capacity after "n" cycles mAh g^{-1} active material	Charge capacity and efficiency after "n" cycles mAh g^{-1} electrode	Average columbic efficiency after "n" cycles, %	Charge capacity after 1010 cycles (mAh g^{-1})	Electrical conductivity (S cm^{-1})
Free-standing	Si(B)CN-rGO	245 (35)	196, 98 (35)	99.2 (1010)	268	0.29
	SiCN-CNT-rGO	275 (35)	220, 98 (35)	95.6 (1010)	197	0.27
	Si(B)CN-CNT-rGO	368 (35)	294, > 99 (35)	99.7 (1010)	357	0.35
	C-rich SiOC	150 (30)	N/A		N/A	
Traditional	MWCNTs [50]	220 (20)	N/A		N/A	
	SiCN-1100 [46]	25 (30)	3.2 (30)		N/A	
	Si(B)CN-CNT [46]	412 (30)	66.29 (30)		N/A	

Further characterization of the free-standing papers involved electrical conductivity measurements using a four-point measurement technique. Conductivity data presented in Table 1 shows Si(B)CN-rGO, SiCN-CNT-rGO, and Si(B)CN-CNT-rGO papers had conductivity of 0.29, 0.27, and 0.35 S cm^{-1}, respectively. The improved conductivity can be attributed to the addition of boron to SiCN microstructure [41] and the incorporation of CNT to form a primary conductive path at the molecular level. [47] These factors, combined with the presence of a conducting rGO network at the macro level, more significantly influenced the cyclic performance of Si(B)CN-CNT-rGO than synthesized PDC, since electron conductivity is essential for efficient Li-ion cycling.

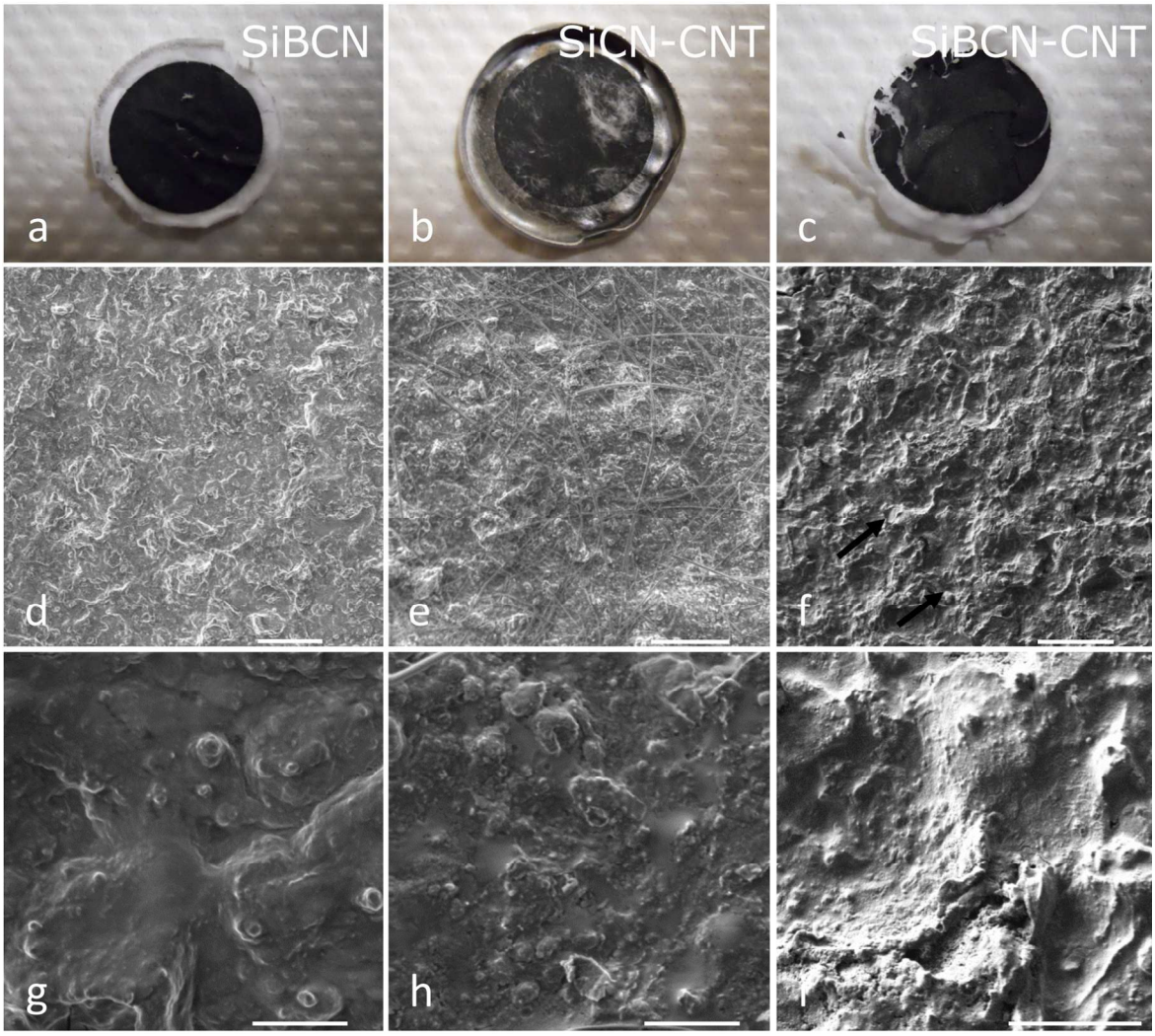

Fig. 3. Digital camera image of (a) Si(B)CN, (b) SiCN-CNT, and (c) Si(B)CN-CNT free-standing composite electrodes after cycling. Corresponding SEM images obtained in the lithiated state after being cycled for 1020 cycles. Scale bar is 40 and 10 micrometers for (d)–(f) and (g)–(i), respectively.

The cells were eventually disassembled in a lithiated state in order to study the change in morphology and chemical structure of the tested PDC due to cycling for more than 1000 cycles. Fig. 3 shows an optical photograph (Fig. 3(a)–(c)), low resolution SEM image (Fig. 3(d)–(f)), and high-resolution SEM image (Fig. 3(g)–(i)) of the lithiated electrode materials. Remarkably, all electrode specimens remained intact with no large or micro surface cracks.

Furthermore, a stable solid electrolyte interface (SEI) layer formation and the presence of glass fiber separator were also observed.

The synthesized PDCs were tested in a two-electrode setup in order to investigate the electrochemical properties of the free-standing electrodes as supercapacitors. The Nyquist plot obtained from EIS is shown in Fig. 4. The high frequency intercept of real impedance axis, which corresponds to electrode-electrolyte interfacial resistance due to electronic and ionic contribution of Si(B)CN-rGO and Si(B)CN-CNT-rGO were identical (0.34 Ω), while that of SiCN-CNT-rGO was slightly higher (0.73 Ω), which suggests its electrical conductivity is lesser due to zero-doping. Among the electrode materials being tested, only Si(B)CN-CNT-rGO showed an almost perfect semicircle at higher frequency, indicating it had the lowest charge-transfer resistance (approximately 2.7 Ω). Therefore, it could be inferred that the interaction of the Si(B)CN-CNT-rGO electrode with the electrolyte promotes adhesion and ion transport to its surface. Also, the shortening of electrons mean-free path due to the conductive network formed between rGO and CNT further enhances the transport of charges within the matrix of Si(B)CN-CNT-rGO during charging and discharging process. [47] The Nyquist plot slopes in the low frequency region indicates a purely capacitive behavior due to the Warburg impedance which arises from ion diffusion frequency dependence and transport in the electrolyte. [59, 60] As shown in the insert of Fig. 4, Si(B)CN-CNT-rGO displays a purely capacitive behavior in a frequency range of 146.5–0.1778 Hz. Beyond this frequency range (> 0.1778 Hz), the Nyquist plot slope gradually deviates from purely capacitive behavior and becomes similar to that of Si(B)CN-rGO.

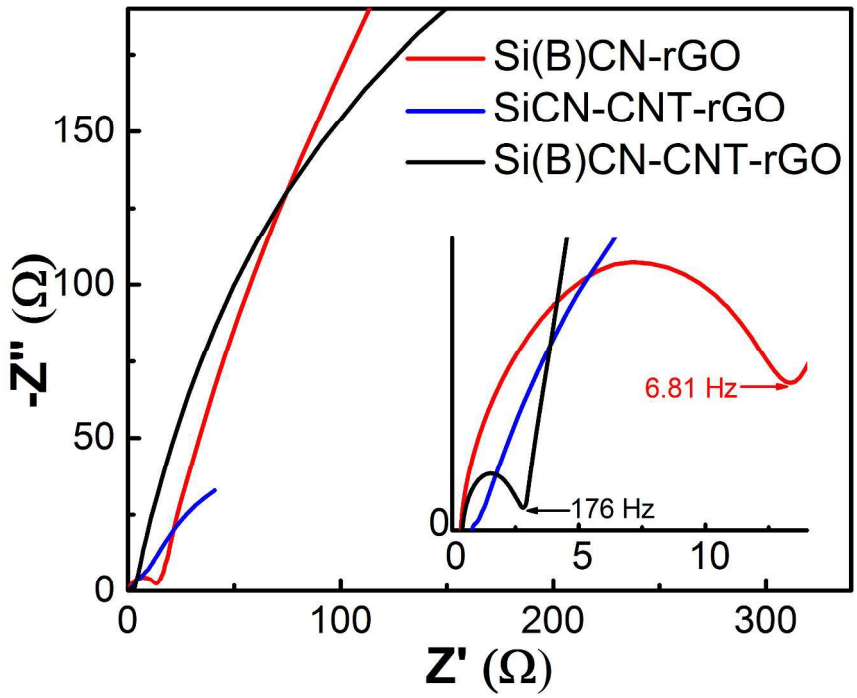

Fig. 4. Nyquist plot for Si(B)CN-rGO, SiCN-CNT-rGO, and Si(B)CN-CNT-rGO electrodes.

Because Si(B)CN-CNT-rGO demonstrated superior electrochemical performance (as suggested from previous experiment), cyclic voltammetric and chronopotentiometric analysis were carried out to elucidate its electrochemical properties as a supercapacitor. Fig. 5(a)–(b) shows the CV and GCD curves of Si(B)CN-CNT-rGO at different scan rates and current densities using 6 M KOH aqueous electrolyte in a two-electrode setup. The CV curves showed a quasi-rectangular shape with increasing area at higher scan rates, indicating good capacitive behavior and reversibility. At a scan rate of 2 mVs^{-1}, a broad pseudo-reduction peak at a potential of 0.37 V was observed, suggesting the masking of impurities in rGO by CNT at high scan rates as reported in the literature. [61] The GCD curve shown in Fig. 5(b) indicates favorable diffusion and adsorption of the electrolyte's ion onto large areas of the porous electrode material which results in an increase in its electrochemical performance as

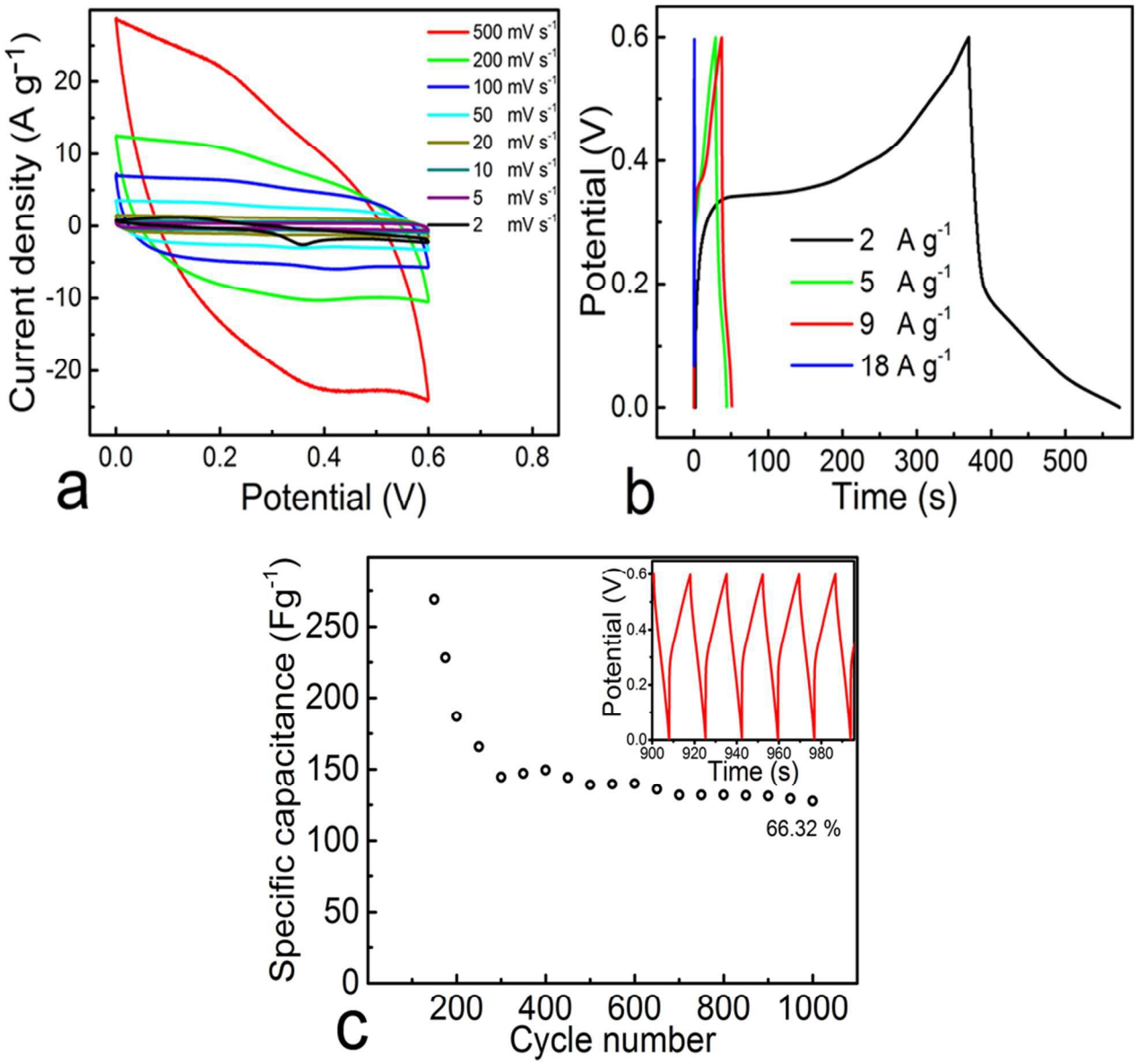

Fig. 5. (a) CV measurement of Si(B)CN-CNT-rGO at different scan rates, (b) GCD plots of Si(B)CN-CNT-rGO recorded at different current densities, (c) cyclic stability test of Si(B)CN-CNT-rGO for 1000 cycles at a current density of 5 A g^{-1} in a potential range of 0–0.6 V (inset shows charge-discharge curves at the last cycle).

an energy storage material. [62, 63] Specific capacitance of Si(B)CN-CNT-rGO was calculated from the slope of its GCD curve using the following expressions:

$$C_s = 2I / (m \times Slope) \quad (1)$$

$$Slope = \Delta V/\Delta t \quad (2)$$

Where Cs, I, m, ΔV, and Δt represent the specific capacitance (F g^{-1}), applied current (A), mass of a single electrode (g), potential window (V) excluding the iR drop during the discharge process and discharge time(s) respectively.

The calculated specific capacitance gave an initial value of 269.02 F g^{-1} (based on the mass of single electrode) at a current density of 5 A g^{-1}. When the cell was subjected to a cycle test of 1000 seconds at same current density, its specific capacitance retention maintained an average value of 127.46 F g^{-1} (66.32 %) (Fig. 5(c)), which was higher than previous capacitance of graphene and CNT-based supercapacitors [64, 65] and lower than that reported by some researchers. [66, 67] The gravimetric capacitance of some ceramic-based supercapacitor electrodes found in the literature are compared in Table 2.

Table 2 Gravimetric capacitance of some carbon-based supercapacitors in comparison to present work

Materials	Electrolytes	Voltage window (V)	Current density/ Scan rate	Specific Capacitance (F g^{-1})	Ref.
SiOCDC	1 M TEA-BF_4 in acetonitrile	-2 to +2	5 A g^{-1}	110	68
SiOCDC	5 M KOH	0.2 to -1.0	1 A g^{-1}	148	69
SiOCDC	1 M TEA-BF_4 in acetonitrile	-1 to +1	10 mVs^{-1}	135	70
SiCDC	1 M TEA-BF_4 in acetonitrile	0 to +2	0.1 A g^{-1}	170	71
Si(B)CN-CNT-rGO	6 M KOH	0 to +6	5 A g^{-1}	269.02	Present work

The obtained value was as expected because the synthesized Si(B)CN-CNT-rGO was a free-standing electrode, devoid of current collectors and other additives (e.g., binders and

conducting materials) that could obscure its true capacitance value. Based on preliminary study results, Si(B)CN-CNT-rGO is a promising material for energy storage applications.

4. Conclusions

We demonstrated the preparation of PDC-CNT-rGO free-standing paper and studied its electrochemical performance as a self-supporting electrode for LIB half-cell and supercapacitor. Among the synthesized PDCs, Si(B)CN-CNT-rGO nanocomposite proved to be the best material with a stable asymmetric cyclic performance, a charge capacity of 206 mAh $g^{-1}_{electrode}$ (82% of the initial capacity retained) even at a current density of 2400 mA g^{-1}. At a current density of 1600 mA g^{-1}, the cell remained stable for 1000 cycles with charge capacity of 52 mAh $g^{-1}_{electrode}$ with 100% cyclic efficiency. Further SEM analysis showed that the electrodes were intact with no visible mechanical damage, even after being cycled for more than 1000 cycles. As an electrode material for a supercapacitor, a maximum specific capacitance of 231.67 F g^{-1} at a current density of 5 A g^{-1} was recorded in a 6 M KOH electrolyte over a voltage window of 0–0.6 V. It is believed that the enhanced electrochemical properties of the Si(B)CN-CNT-rGO electrode is due to boron doping which enhances is conductivity. Also, the inclusion of CNT and rGO into the structure of the electrode material further promotes the electrochemical property of the material by enhancing its porosity and providing a conductive path which shortens electrons mean-free path during charging and discharging processes. Given the possibility of tailoring the properties of PDC-CNT-rGO, robust and clean energy storage materials that will find use as free-standing electrode materials for both LIBs and supercapacitors could be developed.

Acknowledgements

A portion of this research is based on work supported by the National Science Foundation-grant No. 1335862 and 1454151 to G. Singh.

References

1 M. Armand and J. M. Tarascon, *Nature*, 2008, **451**, 652.

2 R. Mukherjee, A. V Thomas, D. Datta, E. Singh, J. Li, O. Eksik, V. B. Shenoy and N. Koratkar, *Nat. Commun.*, 2014, **5**, 1.

3 R. Bhandavat and G. Singh, *J. Phys. Chem. C*, 2013, **117**, 11899.

4 A. S. Aricò, P. Bruce, B. Scrosati, J.-M. Tarascon and W. van Schalkwijk, *Nat. Mater.*, 2005, **4**, 366.

5 E. M. Lotfabad, J. Ding, K. Cui, A. Kohandehghan, W. P. Kalisvaart, M. Hazelton and D. Mitlin, *ACS Nano*, 2014, **8**, 7115.

6 P. V. Kamat, *J. Phys. Chem. Lett.*, 2011, **2**, 242.

7 A. Manthiram, *J. Phys. Chem. Lett.*, 2011, **2**, 176.

8 D. Ahn and R. Raj, *J. Power Sources*, 2011, **196**, 2179.

9 J. O. Besenhard, J. Yang and M. Winter, *J. Power Sources*, 1997, **68**, 87.

10 A. R. Kamali and D. J. Fray, *J. New Mater. Electrochem. Syst.*, 2010, **13**, 147.

11 C. M. Park, J.-H. Kim, H. Kim and H.-J. Sohn, *Chem. Soc. Rev.*, 2010, **39**, 3115.

12 W. J. Zhang, *J. Power Sources*, 2011, **196**, 13.

13 H. Wu and Y. Cui, *Nano Today*, 2012, **7**, 414.

14 M. W. Verbrugge and Y. T. Cheng, *Electrochem. Soc. Trans.*, 2008, **16**, 127.

15 M. W. Verbrugge and Y. T. Cheng, *J. Electrochem. Soc.*, 2009, **156**, A927.

16 M. H. Park, M. G. Kim, J. Joo, K. Kim, J. Kim, S. Ahn, Y. Cui and J. Cho, *Nano Lett.*, 2009, **9**, 3844.

17 T. Song, J. Xia, J. H. Lee, D. H. Lee, M. S. Kwon, J. M. Choi, J. Wu, S. K. Doo, H. Chang, W. Il Park, D. S. Zang, H. Kim, Y. Huang, K. C. Hwang, J. A. Rogers and U. Paik, *Nano Lett.*, 2010, **10**, 1710.

18 L. Y. Beaulieu, K. W. Eberman, R. L. Turner, L. J. Krause and J. R. Dahn, *Electrochem. Solid-State Lett.*, 2001, **4**, A137.

19 T. D. Hatchard and J. R. Dahn, *J. Electrochem. Soc.*, 2004, **151**, A838.

20 R. Deshpande, Y. T. Cheng and M. W. Verbrugge, *J. Power Sources*, 2010, **195**, 5081.

21 U. Kasavajjula, C. Wang and A. J. Appleby, *J. Power Sources*, 2007, **163**, 1003.

22 R. Ruffo, S. S. Hong, C. K. Chan, R. A. Huggins and Y. Cui, *J. Phys. Chem. C*, 2009, **113**, 11390.

23 D. Aurbach, *J. Power Sources*, 2000, **89**, 206.

24 J. Luo, X. Zhao, J. Wu, H. D. Jang, H. H. Kung and J. Huang, *J. Phys. Chem. Lett.*, 2012, **3**, 1824.

25 S. Sarkar, Z. Gan, L. An and L. Zhai, *J. Phys. Chem. C*, 2011, **115**, 24993.

26 R. Peña-Alonso, G. Mariotto, C. Gervais, F. Babonneau and G. D. Soraru, *Chem. Mater.*, 2007, **19**, 5694.

27 G. D. Sorarù and D. Suttor, *J. Sol-Gel Sci. Technol.*, 2007, **14**, 69.

28 S. Sarkar, J. Zou, J. Liu, C. Xu, L. An and L. Zhai, *ACS Appl. Mater. Interfaces*, 2010, **2**, 1150.

29 A. Saha, R. Raj and D. L. Williamson, *J. Am. Ceram. Soc.*, 2006, **89**, 2188.

30 J. Bill and F. Aldinger, *Adv. Mater.*, 1995, **7** 775.

31 M. Weinmann, J. Schuhmacher, H. Kummer, S. Prinz, J. Peng, H. J. Seifert, M. Christ, K. Muller, J. Bill and F. Aldinger, *Chem. Mater.*, 2000, **12**, 623.

32 H. Fukui, N. Nakata, K. Dokko, B. Takemura, H. Ohsuka, T. Hino and K. Kanamura, *ACS Appl. Mater. Interfaces*, 2011, **3**, 2318.

33 J. Shen and R. Raj, *J. Power Sources*, 2011, **196**, 5945.

34 D. Ahn and R. Raj, *J. Power Sources*, 2010, **195**, 3900.

35 Y. Feng, *Electrochim. Acta*, 2010, **55**, 5860.

36 M. Graczyk-Zajac, G. Mera, J. Kaspar and R. Riedel, *J. Eur. Ceram. Soc.*, 2010, **30**, 3235.

37 J. Kaspar, G. Mera, A. P. Nowak, M. Graczyk-Zajac and R. Riedel, *Electrochim. Acta*, 2010, **56**, 174.

38 V. Liebau-Kunzmann, C. Fasel, R. Kolb and R. Riedel, *J. Eur. Ceram. Soc.*, 2006, **26**,

3897.

39 D. Su, Y. L. Li, Y. Feng and J. Jin, *J. Am. Ceram. Soc.*, 2009, **92**, 2962.

40 H. Tamai, H. Sugahara and H. Yasuda, *J. Mater. Sci. Lett.*, 2000, **19**, 53.

41 A. M. Hermann, Y. T. Wang, P. A. Ramakrishnan, D. Balzar, L. An, C. Haluschka and R. Riedel, *J. Am. Ceram. Soc.*, 2001, **84**, 2260.

42 Y. Feng, G. X. Du, X. J. Zhao and E. C. Yang, *J. Appl. Electrochem.*, 2011, **41**, 999.

43 Y. Feng and G. D. X. Zhao, *Int. J. Electrochem. Sci.*, 2012, **7**, 3135.

44 M. Graczyk-Zajac, C. Fasel and R. Riedel, *J. Power Sources*, 2011, **196**, 6412.

45 R. Kolb, C. Fasel, V. Liebau-Kunzmann and R. Riedel, *J. Eur. Ceram. Soc.*, 2006, **26**, 3903.

46 R. Bhandavat and G. Singh, *J. Am. Ceram. Soc.*, 2012, **95**, 1536.

47 Z. Fan, J. Yan, L. Zhi, Q. Zhang, T. Wei, J. Feng, M. Zhang, W. Qian and F. Wei, *Adv. Mater.*, 2010, **22**, 3723.

48 J. William, S. Hummers and R. E. Offeman, *J. Am. Chem. Soc.*, 1958, **80**, 1339.

49 L. David, A. Feldman, E. Mansfield, J. Lehman and G. Singh, *Sci. Rep.*, 2014, **4**, 4311.

50 R. Bhandavat, W. Kuhn, E. Mansfield, J. Lehman and G. Singh, *ACS Appl. Mater. Interfaces*, 2012, **4**, 11.

51 L. David, R. Bhandavat, U. Barrera and G. Singh, *Nat. Commun.,* 2016, **7,** 10998.

52 L. David, and G. Singh, *J. Phys. Chem. C*, 2014, **118**, 28401.

53 B. J. Landi, R. A. Dileo, C. M. Schauerman, C. D. Cress, M. J. Ganter and R. P. Raffaelle, *J. Nanosci. Nanotechnol.*, 2009, **9**, 3406.

54 R. Bhandavat and G. Singh, *ACS Appl. Mater. Interfaces*, 2012, **4**, 5092.

55 T. Zheng, W. R. McKinnon, and J. R. Dahn, *J. Electrochem. Soc.*, 1996, **148**, 2137.

56 R. Bhandavat and G. Singh, *J. Am. Chem. Soc.*, 2012, **95**, 1536.

57 S. Bernard, M. Weinmann, P. Gerstel, P. Mielea and F. Aldingerb, *J. Mater. Chem.*, 2005,**15**, 289.

58 D. R. Dreyer, S. Park, C. W. Bielawski and R. S. Ruoff, *Chem. Soc. Rev.*, 2010, **39**, 228.

59 H. An, Y. Li, P. Long, Y. Gao, C. Qin, C. Cao, Y. Feng and W. Feng, *J. Power Sources*, 2016, **312**, 146.

60 M. S. Kolathodi, S. N. Rao, T. S. Natarajan and G. Singh, *J. Mater. Chem. A*, 2016, **4**, 7883.

61 M. Pumera, A. Ambrosi and E. L. Chang, *Chem. Sci.*, 2012, **3**, 3347.

62 M. S. Kolathodi, M. Palei and T. S. Natarajan, *J. Mater. Chem. A*, 2015, **3**, 7513.

63 M. S. Kolathodi and T. S. Natarajan, *Scr. Mater.*, 2015, **101**, 84.

64 Z. S. Wu, A. Winter, L. Chen, Y. Sun, A. Turchanin, X. Feng and K. Müllen, *Adv. Mater.*, 2012, **24**, 5130.

65 Y. Zhang, C. Liu, B. Wen, X. Song and T. Li, *Mater. Lett.*, 2011, **65**, 49.

66 W. Wang, S. Guo, M. Penchev, I. Ruiz, K. N. Bozhilov, D. Yan, M. Ozkan and C. S. Ozkan, *Nano Energy*, 2013, **2**, 294.

67 Q. Cheng, J. Tang, J. Ma, H. Zhang, N. Shinya and L. C. Qin, *Phys. Chem. Chem. Phys.*, 2011, **13**, 17615.

68 A. Meier, M. Weinberger, K. Pinkert, M. Oschatz, S. Paasch, L. Giebeler, H. Althues, E. Brunner, J. Eckert and S. Kaskel, *Microporous Mesoporous Mater.*, 2014, **188**, 140.

69 L. Duan, Q. Ma, L. Mei, and Z. Chen, *Microporous Mesoporous Mater.*, 2015, **202**, 97.

70 A. Tolosa, B. Krüner, N. Jäckel, M. Aslan, C. Vakifahmetoglu and V. Presser, *J. Power Sources*, **313**, 178.

71 Y. Korenblit, M. Rose, E. Kockrick, L. Borchardt, A. Kvit, S. Kaskel and G. Yushin, *Acs Nano*, **4**, 1337.

Abstract

We study synthesis and electrochemical performance of molecular precursor-derived ceramic (PDC)/carbon nanotube-embedded graphene self-supporting composite papers as Li-ion battery and supercapacitor electrodes. The composite papers are prepared using vacuum filtration of PDC-graphene oxide (GO) dispersion, followed by thermal reduction at 500 ^{o}C. Tested as Li-ion battery electrode, the composite papers deliver reversible capacity as high as 300 mAh g^{-1} (normalized with respect to total mass of electrode) with negligible capacity loss after 1000 charge/discharge cycles. Boron-doped silicon carbon nitride (Si(B)CN) outperforms its undoped counterpart (SiCN) in terms of rate capability, cyclic stability, and coulombic efficiency. Among the PDC materials analyzed, Si(B)CN-CNT-rGO demonstrates the lowest ohmic resistance and highest specific capacitance of approximately 269.52 F g^{-1} at a current density of 5 A g^{-1}, making it a promising electrode material for electrochemical energy storage applications.